Received: 18 October 2023 | Revised: 23 April 2024 | Accepted: 2 May 2024

DOI: 10.1002/jrs.6684

RESEARCH ARTICLE

Journal of RAMAN SPECTROSCOPY WILEY

Raman scattering of $Ti_xV_{1-x}O_2$ thin films on (110) rutile TiO_2 in the low and high temperature phase adjacent to the metal–insulator transition

Florian Kuhl[1] | **Hao Lu**[1] | **Martin Becker**[1] | **Limei Chen**[1] | **Yonghui Zheng**[2] | **Angelika Polity**[1] | **Zaoli Zhang**[2] | **Yunbin He**[3] | **Peter J. Klar**[1]

[1]Institute of Experimental Physics I and Center for Materials Research (ZfM/LaMa), Justus Liebig University Giessen, Giessen, Germany

[2]Erich Schmid Institute of Materials Science, Austrian Academy of Sciences, Leoben, Austria

[3]Key Laboratory of Green Preparation and Application for Functional Materials, Ministry of Education, School of Materials Science Engineering, Hubei University, Wuhan, People's Republic of China

Correspondence
Hao Lu, Institute of Experimental Physics I and Center for Materials Research (ZfM/LaMa), Justus Liebig University Giessen, Heinrich-Buff-Ring 16, DE-35392 Giessen, Germany.
Email: hao.lu@physik.uni-giessen.de

Zaoli Zhang, Erich Schmid Institute of Materials Science, Austrian Academy of Sciences, Leoben 8700, Austria.
Email: Zaoli.Zhang@oeaw.ac.at

Yunbin He, Key Laboratory of Green Preparation and Application for Functional Materials, Ministry of Education, School of Materials Science Engineering, Hubei University, Wuhan 430062, People's Republic of China.
Email: ybhe@hubu.edu.cn

Funding information
National Natural Science Foundation of China, Grant/Award Numbers: 11975093, 51572073, 62274057; Sino-German

Abstract

Vanadium dioxide (VO_2) undergoes a reversible first-order metal-to-insulator transition (MIT) from a high-temperature metallic phase to a low-temperature insulating phase at a critical temperature T_c of 68°C. The MIT is accompanied by a structural phase transition. In addition to the metallic high-temperature rutile phase, several insulating phases may be involved depending on doping, interfacial stress, or external stimuli. Unambiguously identifying the crystal phases involved in the phase transition is of key interest from the point of view of application as well as fundamental science. We study the impact of Ti doping of VO_2 thin films on (110) rutile TiO_2 substrates. We conduct a careful analysis of structural properties by combining results of x-ray diffraction, Raman spectroscopy, and transmission electron microscopy. The transition temperature T_c of the deposited thin films decreases with increasing Ti-content. All our thin film samples undergo a structural phase transition from the monoclinic M_1-phase to the rutile R-phase with increasing temperature without passing the intermediate monoclinic M_2-phase. A careful analysis of polarization and angle-dependent Raman data reveals that, above T_c, the unit cell of the high-temperature rutile $Ti_xV_{1-x}O_2$ phase is aligned with that of the rutile TiO_2 substrate whereas, below T_c, 180°-domains of the M_1-phase of $Ti_xV_{1-x}O_2$ are observed. The structural relationship between TiO_2 substrate and the high respective low-temperature phase of the $Ti_xV_{1-x}O_2$ determined by Raman spectroscopy is in excellent agreement with TEM results on these samples. Raman spectroscopy is a powerful tool for studying structural changes of VO_2-based samples in the vicinity of MIT.

KEYWORDS

metal–insulator transition, phase transition, Raman spectroscopy, titanium doping, vanadium-dioxide-based thin films

Mobility Program, Grant/Award Number: M-0764; Natural Science Foundation of Hubei Province, Grant/Award Numbers: 2019CFA006, 2021EHB005, 2022EHB023; Program for Science and Technology Innovation Team in Colleges of Hubei Province, Grant/Award Number: T201901; China Scholarship Council; German BMBF, Grant/Award Number: 03VP09691; Austrian Innovation Fund, Grant/Award Number: €OAW 4023; DFG, Grant/Award Number: 510965362

1 | INTRODUCTION

The family of binary oxides is huge and exhibits many interesting properties making its members promising candidate materials for a wide range of applications.[1–3] Members of the family may be insulators, semiconductors, or metals exhibiting all sorts of band gaps. However, in particular, transition metal oxides have far more to offer due to their partially filled metal d-shells and strong electron–electron correlations. Additional interesting properties such as superconductivity, ferromagnetism, antiferromagnetism, thermochromic or electrochromic behavior, and ion conductivity result, which offer great potential for novel applications.[4–6] The phase diagrams of binary oxides M_mO_n are rather rich (m and n are integer values for stoichiometric material). Various crystalline phases may exist either exhibiting different stoichiometries (i.e., m: n ratio) or even possessing the same stoichiometry. In many cases, the unit cells contain several formula units and the differences between phases result from tiny distortions of essentially the same atomic arrangement. Furthermore, structural properties as well as electrical, magnetic, or other properties are tunable by doping and alloying and may be easily manipulated by external stimuli. Thus, a full microscopic understanding of the tunability of the properties by doping and alloying is of paramount importance for employing these materials in thin-film or multilayer devices.

As the properties of these materials are so easily varied, it is essential to also account for a possible influence of the surrounding layers in terms of induced strain or band bending or doping by defect diffusion. A good starting point for assessing the impact of the surrounding layers is always a thorough structural characterization of the deposited material. X-ray diffraction (XRD) is widely used as a standard tool for assessing the structural properties of polycrystalline or crystalline thin films. However, Raman spectroscopy, though more cumbersome, can be advantageous compared to standard XRD, in particular in some cases where candidate structures possess a large number of atoms per unit cell and are of low symmetry. An example is the unambiguous identification of monoclinic Sn_3O_4 as an intermediate phase between SnO and SnO_2. In this case, it is difficult to differentiate between the monoclinic structures of Sn_2O_3 and Sn_3O_4 by a standard diffraction analysis whereas the Raman spectra of the two phases can be easily distinguished.[7]

Vanadium oxides also belong to the family of binary metal oxides. Vanadium in these compounds may exhibit four different oxidation states (V^{2+}, V^{3+}, V^{4+}, or V^{5+}) yielding several binary phases with complex properties. Materials may even contain V in more than one of these four oxidation states, for example, some of the Magnéli phases V_mO_n ($n = 2\,m - 1$, $m > 1$) or the Wadsley phases V_mO_n ($n = 2\,m + 1$, $m > 1$). The Wadsley phases can be considered as vanadium oxides arising from mixing VO_2 with the Magnéli phases. The Wadsley phases V_6O_{13}, V_3O_7, and V_2O_5 exhibit average oxidation states in the range between V^{4+} and V^{5+}. The Magnéli phases V_2O_3 and VO_2 only exhibit a single oxidation state of V^{3+} and V^{4+}, respectively. Raman spectroscopy has proven to be a powerful tool for distinguishing different V_mO_n phases.[8–10]

VO_2 shows a metal-to-insulator transition (MIT) with an abrupt change in structural, optical, and electrical properties.[11,12] The MIT transition in stoichiometric bulk VO_2 takes place at $T_c \cong 68°C$ and is accompanied by a structural phase transition from the low-temperature monoclinic insulating phase (M_1-phase) into the high-temperature rutile metallic phase (R-phase). Applying strain or doping may alter the situation considerably.[13,14] When incorporating acceptors on the V site or when applying tensile strain along the direction of the rutile c-axis of VO_2, the critical temperature T_c of the MIT is shifted to higher temperatures in single crystalline or polycrystalline stoichiometric $Ti_xV_{1-x}O_2$ for $x > 0$.[15–19] The accompanying structural phase transitions take place in two steps in the vicinity of the MIT. With increasing temperature, the insulating monoclinic M_1-phase turns into another insulating monoclinic phase (M_2-phase), which then transforms into the metallic rutile phase. The properties of polycrystalline, crystalline binary or alloyed VO_2 thin films on different substrates or the embedding

of such films into layered structures may induce lattice strain, preferential crystalline orientation, domain formation, or unintentional doping. These structural changes may significantly alter the properties related to the MIT as well as the crystalline phases involved.[14,20–22]

The occurrence of the M_2-phase in doped or non-stoichiometric $Ti_xV_{1-x}O_2$ is not guaranteed during the phase transition. Doping can be categorized as hole doping (e.g. with Al, Cr, Fe, Ga) or electron doping (e.g. Nb, Mo, W, or oxygen vacancies V_O). Electron doping leads to a significant destabilization of the insulating M_1-phase as the doping concentration increases in the solid solution. As a consequence, the material becomes metallic at a lower T_C. Furthermore, the M_2 phase is suppressed and the phase transition of electron-doped $Ti_xV_{1-x}O_2$ occurs between the insulating M_1 phase and the metallic R phase only. In the case of hole doping, the impact on the MIT temperature is opposite to that of electron doping. This means the MIT temperature T_C typically increases and the M_2-phase occurs as an intermediate phase between M_1 and R-phase. Furthermore, the temperature window where the M_2 phase occurs widens. About 50 years ago, an additional insulating phase with symmetry and magnetic properties distinct from those of M_1 was identified in $Fe_xV_{1-x}O_2$ and $Cr_xV_{1-x}O_2$ solid solutions.[23,24] It is now well-established that two new insulating phases, M_2 and T, may be observed when doping VO_2 with small amounts of Cr, Al, Fe, or Ga.[23–28] The M_2-R and T-M_2 transition both are first-order transitions, while the M_1-T transition is essentially continuous. Furthermore, binary VO_2 may occur in several different crystalline phases.[29] These VO_2 phases often are hard to discern in the case of VO_2-based polycrystalline or crystalline thin films by employing standard XRD analysis whereas their Raman spectra are easily distinguishable.[8,14]

Here, we focus on the structural properties of crystalline $Ti_xV_{1-x}O_2$ thin films on (110) TiO_2 substrates in the vicinity of the MIT as a function of Ti concentration x. In particular, we employ temperature, angle, and polarization-dependent Raman measurements as a tool for exploring the structural properties of such samples. A thorough comparison of these results with those obtained by transmission electron microscopy (TEM) and XRD on the same samples allows us to assess the capabilities of Raman spectroscopy as a tool for structural characterization.

2 | EXPERIMENTAL DETAILS

The Ti-doped VO_2 thin films were deposited onto TiO_2 (110) single crystalline substrates by pulsed laser deposition (PLD) using a KrF excimer laser (Lambda Physik COMPEX PRO 205F, $\lambda = 248$ nm). A rotating ceramic VO_2 target was used in the deposition process. Prior to growing the film, the substrate was heated up to 750°C for 10 minutes inside the deposition chamber at a background pressure of 5×10^{-4} Pa. The substrate was cooled down to 600°C before commencing the actual growth process. During deposition of the thin film, the energy of a laser pulse was kept to 600 mJ and the pulse repetition rate was 5 Hz. High-purity O_2 as reactive gas was introduced into the deposition chamber while the pressure was constantly kept at 1 Pa. The deposition rate of the films was 8 nm/min. Alloying of the thin films with Ti was achieved by attaching high-purity Ti sheets to the target. The coverage of the target with the Ti sheets determines the degree of doping of the VO_2 thin film. In addition to the undoped sample, we realized $Ti_xV_{1-x}O_2$ thin films with alloying levels of 0%, 1%, 2.5%, 3.3%, 4%, 5.3%, and 8.6%. The pure VO_2 film has a thickness of approximately 90 nm only, while the remaining doped films have a thickness of about 300 nm, estimated from the film deposition rate.

Angle and temperature-dependent Raman spectroscopic measurements were performed using a Renishaw inVia Raman microscope system. Series of Raman spectra in the temperature range between 0°C and 80°C were recorded using a Linkam THMS 600 temperature stage. The spectra were taken in backscattering geometry with 514 nm excitation provided by an Ar-ion laser. Excitation and scattered light passed through a long-distance objective (50 ×, Olympus, NA = 0.45). The Rayleigh scattered laser light was rejected by an edge filter enabling the measurement of the Stokes Raman scattered light down to 100 cm^{-1}. The laser power on the sample was 1.9 mW and the spot size was about 1 μm. Using polarization optics in the beam path allowed us to measure Raman spectra in parallel and crossed polarization configuration of laser and Raman scattered light. Angle-dependent measurements were realized on the same spot on the sample by rotating the polarizer arrangement in the beam path.

The sample's electric resistance as a function of temperature was measured using a linear four-contact geometry and a heater stage. Either tungsten carbide or steel needles with a diameter of 0.5 mm were used as contacts. The total force applied to the needles was about 5 to 16 N. The distance between probes was 1 ± 0.01 mm. The resistance measurements were performed in auto-ranging mode. The heating rate was 2°C/min.

X-ray diffraction (XRD) traces were recorded with Rigaku SmartLab diffractometer and Panalytical X'Pert Pro MRD setups using the Cu-Kα line and an additional sample heater to reach temperatures between room temperature and 80°C. The scanning step was 0.02° in a setup with a minimum step size of 10 arc sec. Transmission electron microscopy (TEM) was performed on cross-sectional samples in dark-field mode in scanning TEM (STEM) mode using a JEM Grand ARM300F system.

Details of the sample preparation and the measurement procedure are described by Zheng et al.[30]

3 | EXPERIMENTAL RESULTS AND DISCUSSION

The monoclinic and the rutile structures of VO_2 are strongly related. Furthermore, there are two modifications of the VO_2 monoclinic structure, the so-called M_1 and the M_2-phase, which play a role in the context of the MIT of VO_2 and VO_2-based materials.[31] As we will see in the discussion of Figures 1 and 2, we will be confronted with the M_1-phase only and do not observe the M_2-phase as an intermediate phase in the vicinity of the MIT. Therefore, we will focus mainly on the structural relationship between the M_1 and the R-phase of VO_2.

The unit cell of M_1-VO_2 contains four VO_2 structural units. At the phase transition temperature to rutile R-VO_2, the chains of VO_6 octahedra, which are paired and tilted, forming zigzag chains along the monoclinic *a*-axis (which becomes the rutile *c*-axis at the phase transition), realign. They become equally spaced leading to the higher tetragonal symmetry. The higher symmetry reduces the size of the unit cell such that it now contains two VO_2 structural units only, i.e. the rutile unit cell is half the size of the monoclinic unit cell of the M_1-phase. The structural phase transition is also accompanied by the transition from insulating to metallic behavior. In contrast, the insulating M_2-phase (which often occurs in samples uniaxially strained along the monoclinic a-axis or in the case of p-doping) exhibits two distinctly different vanadium sublattices. In the one sublattice, the vanadium atoms are paired along the monoclinic *a*-axis but not tilted, and in the other sublattice they are tilted perpendicular to the *a*-axis but unpaired. The monoclinic cell of the M_2-phase of $C_{2/m}$ symmetry contains eight VO_2 structural units.[14,32–34]

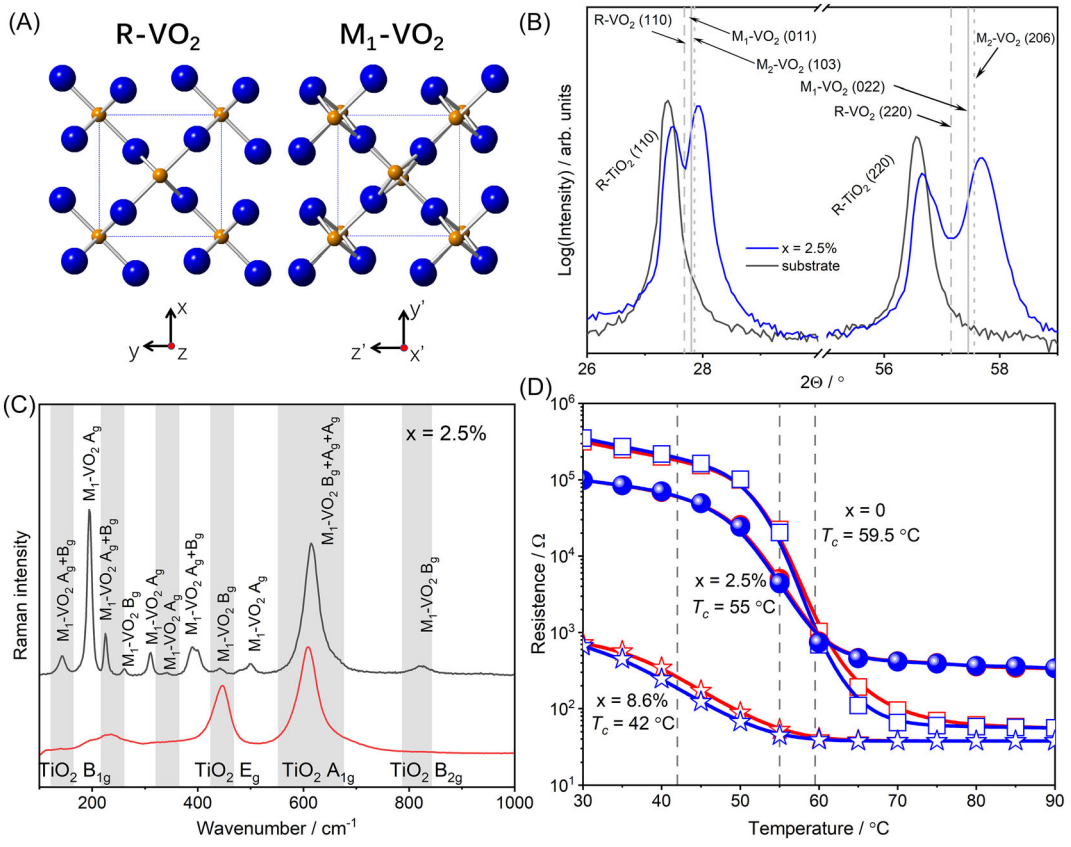

FIGURE 1 (A) Unit cell of R-VO_2 (on the left) and the corresponding half of the unit cell of M_1-VO_2 (on the right) seen along the rutile $\vec{c}_r$-axis (|| Cartesian coordinate *z*) and the corresponding monoclinic $\vec{a}_m$-axis (||Cartesian coordinate *x*'), respectively. (B) θ-2θ XRD traces were recorded at room temperature of a VO_2 thin film with 2.5% Ti deposited on (110) TiO_2 substrate and the plain substrate. The θ-2θ-scan of the thin film reveals signals in addition to that of the TiO_2 substrate, which can be assigned either to r-VO_2 or M_1-VO_2. (C) Room-temperature Raman spectrum of a VO_2 thin film with 2.5% of Ti. The spectral regions where signals of the rutile TiO_2 substrate may affect the Raman signatures of the $Ti_xV_{1-x}O_2$ thin films are indicated by a grey background. Raman bands, which may be assigned to A_g and B_g modes of the M_1-VO_2:Ti are indicated. (D) Temperature-dependent resistance measurements of three $Ti_xV_{1-x}O_2$ thin films on (110) TiO_2 of different *x* showing a step-like increase with decreasing temperature indicative for the metal-to-insulator transition.

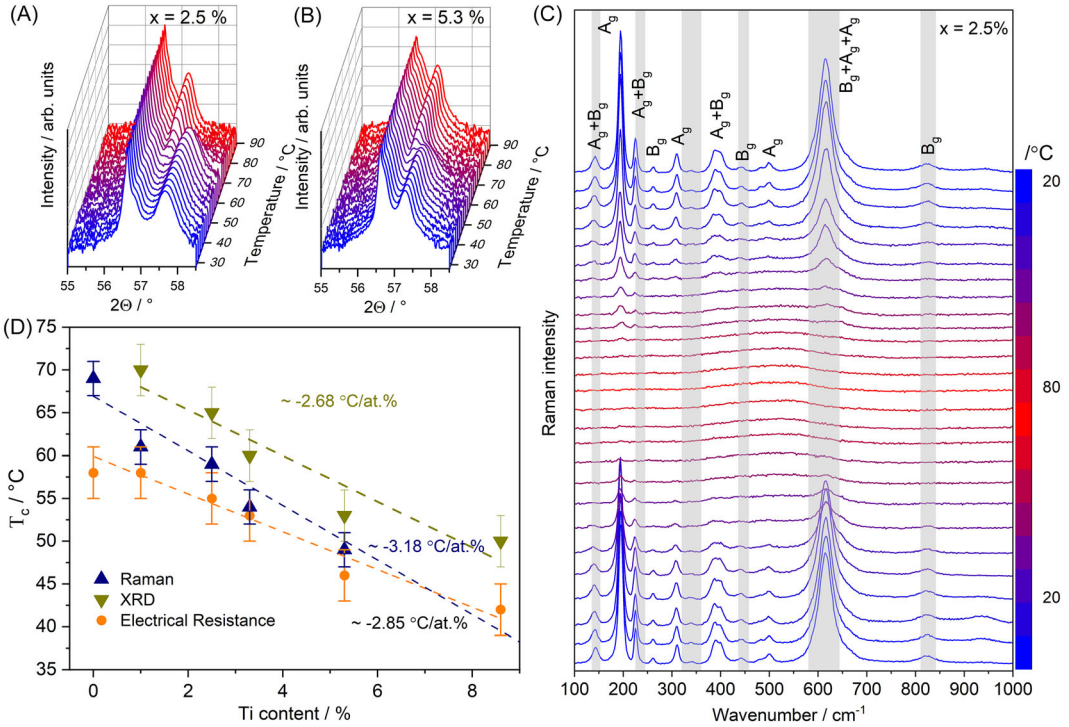

FIGURE 2 (A,B) Series of θ-2θ-scans as a function of temperature between 30 and 90°C for $Ti_xV_{1-x}O_2$ with $x = 2.5\%$ and 5.3%, respectively. (C) Series of Raman spectra of a $Ti_{0.025}V_{0.975}O_2$ thin film on TiO_2 substrate in the temperature range between 20 and 80°C where the structural phase transition occurs. (D) Dependence of the phase transition temperature T_c on Ti-content x. The T_c-values are determined by analyzing temperature-dependent measurements of the resistance, of θ-2θ XRD traces, and of Raman spectra.

Figure 1A shows views of the unit cell of R-VO_2 (on the left) and the corresponding half of the unit cell of M_1-VO_2 (on the right) seen along the rutile $\vec{c}_r$-axis (|| Cartesian coordinate z) and the corresponding monoclinic $\vec{a}_m$-axis (||Cartesian coordinate x'), respectively. The views of the two crystal structures underline again that only a small displacement of the atoms occurs during phase transformation. The lattice constants and lattice angles of the two VO_2 crystalline phases are strongly correlated and given in Table 1. However, two different domains of the monoclinic M_1-phase (denoted by $i = 1, 2$) may be formed by the atomic displacement due to the fact that β_m is not a right angle. The following relations hold for the Cartesian coordinate system (x_i', y_i', z_i') of the unit cell of domain i of the monoclinic phase and the Cartesian coordinate system (x,y,z) of the rutile phase:

$$\begin{aligned}\vec{a}^{\,1}{}_{M1} &\simeq 2\vec{c}_R \| z \| x_1' \quad \vec{b}^{\,1}{}_{M1} \\ &\simeq \vec{a}_R \| x \| y_1' \quad \vec{c}_{M1} \nparallel \vec{b}_r \| y \| z_1'. \\ \vec{a}^{\,2}{}_{M1} &\simeq -2\vec{c}_R \| -z \| x_2' \quad \vec{b}^{\,2}{}_{M1} \\ &\simeq -\vec{b}_R \| -y \| y_2' \quad \vec{c}^{\,2}{}_{M1} \nparallel -\vec{a}_R \| -x \| z_2'.\end{aligned} \tag{1}$$

TABLE 1 Lattice parameters for monoclinic M_1 and rutile R-VO_2 unit cells. The data is taken from Longo and Kierkegaard[35] (monoclinic structure, four structural units) and McWhan[36] (rutile structure, two structural units).

M_1-VO_2	R-VO_2
$a_{M1} = 5.7517$ Å	$a_R = 4.5546$ Å
$b_{M1} = 4.5378$ Å	$b_R = 4.5546$ Å
$c_{M1} = 5.3825$ Å	$c_R = 2.8514$ Å
$\alpha_{M1} = 90°$	$\alpha_R = 90°$
$\beta_{M1} = 122.646°$	$\beta_R = 90°$
$\gamma_{M1} = 90°$	$\gamma_R = 90°$
$V_{M1} = 118.2899$ Å^3	$V_R = 59.15020$ Å^3

In particular, z_1' (z_2') is not parallel to $\vec{c}^{\,1}{}_{M1}$ ($\vec{c}^{\,2}{}_{M1}$) as the angle between $\vec{c}^{\,1}{}_{M1}$ and $\vec{b}_R$ ($\vec{c}^{\,2}{}_{M1}$ and $-\vec{a}_R$) is about 32.6°. Thus, z_i' is given by the projection of $\vec{a}^{\,i}{}_{M1}$ onto the normal vector of the plane spanned by $\vec{a}^{\,i}{}_{M1}$ and $\vec{b}^{\,i}{}_{M1}$. For example, Shibuya and Sawa observed such 180°-domains for VO_2 grown on (110) rutile MgF_2.[22] The following transformation holds between the two Cartesian coordinate systems of the two monoclinic domains and the coordinate system of the rutile phase

$$(x_i', y_i', z_i')^T = \mathfrak{I}_i (x\,y\,z)^T \quad (2)$$

where the transformation matrices $\mathfrak{I}_i$ are given by

$$\mathfrak{I}_1 = \begin{pmatrix} 0 & 0 & 1 \\ 1 & 0 & 0 \\ 0 & 1 & 0 \end{pmatrix} \mathfrak{I}_2 = \begin{pmatrix} 0 & 0 & -1 \\ 0 & -1 & 0 \\ -1 & 0 & 0 \end{pmatrix}. \quad (3)$$

We will make use of this transformation when analyzing the angle dependence of the Raman signals of the $Ti_xV_{1-x}O_2$ samples at room temperature. More information about the relationships between the different Cartesian coordinate systems used can be found in Figure S1. It shows spectra of $Ti_xV_{1-x}O_2$ thin films of different x for the same orientation of the substrate and defined parallel and crossed polarization geometries.

The number of atoms in the unit cell, their positions, and the crystalline symmetry determine the number of Raman-active vibrational modes. The monoclinic M_1-structure of VO_2 corresponds to the space group $P2_1/c$[36] whereas the R-structure of VO_2 belongs to the space group $P4_2/mnm$.[37] Group theory yields 18 Raman active modes for the M_1-structure, which comprise 9 A_g vibrations and 9 B_g vibrations.[10] In contrast, the R-structure of VO_2 because of its higher symmetry and half the number of atoms per unit cell only exhibits four signals of the five Raman active modes, an A_{1g}, a B_{1g}, a B_{2g}, and a double-degenerate E_g vibration. R-VO_2 is of the same structure as rutile TiO_2. The vibrational patterns of the modes are primarily given by motions of the oxygen atoms in the unit cell,[10] as described by Frank et al.[38]

Figure 1B depicts θ-2θ XRD traces recorded at room temperature of a VO_2 thin film with 2.5% Ti deposited on (110) TiO_2 substrate and of the plain substrate. The composition of the $Ti_xV_{1-x}O_2$ films was determined by X-ray photoelectron spectroscopy (XPS), see Figure S6. The θ-2θ-scan of the $Ti_{0.025}V_{0.975}O_2$ thin film reveals in both ranges a signal in addition to that of the TiO_2 substrate. The signals originating from the $Ti_{0.025}V_{0.975}O_2$ thin film are located at 27.75° and 57.35°, respectively. The crystal structures of the TiO_2 substrate, the M_1, M_2, and R-modification of the crystalline VO_2:Ti thin film are very similar. Thus, the XRD feature at 27.75° next to that of the TiO_2 substrate may originate either from the diffraction of the R-VO_2 $(110)_r$ planes or the (011) M_1-VO_2 planes or a corresponding reflex of the M_2-phase. The same holds for the XRD feature at 57.35°, which is due to second-order diffraction. Thus, the θ-2θ trace alone does not allow us to distinguish whether the VO_2:Ti features are due to the M_1-phase, the M_2-phase, or the R-phase or the presence of a mixture of these VO_2 phases, in particular when strain is present in the films or the film is a VO_2-based alloy.

The situation is different in the case of the room-temperature Raman spectra of the VO_2:Ti thin films on (110) TiO_2 substrate. Figure 1C shows a room-temperature Raman spectrum of a VO_2 thin film with 2.5% Ti. At first sight, the Raman spectrum seems to be dominated by the Raman features of the rutile TiO_2 substrate. The Raman spectrum of rutile TiO_2 exhibits four one-phonon Raman signals at 141, 447, 612, and 826 cm^{-1}, which have been assigned to the B_{1g}, E_g, A_{1g}, and B_{2g} modes, respectively.[39–41] Additional, much broader modes centered at 235 cm^{-1} and between 320 and 360 cm^{-1} also may occur in Raman spectra of rutile TiO_2. Their origin is not quite clear; they may be disorder-induced or due to combination modes, i.e., higher-order Raman processes.[41] All the regions where TiO_2 Raman signals may contribute to the spectrum are indicated by a grey background in the graph. However, several additional sharp Raman signals are clearly observable in the room-temperature Raman spectrum outside the grey regions of the graph, e.g., the prominent modes at 194 and 224 cm^{-1}, as well as a number of smaller signals in the range up to 600 cm^{-1}. A comparison with spectra in the literature reveals that these modes belong to the M_1-phase of VO_2.[8,22,42,43] Modes at 137, 194, 310, 340, 499, 612, and 663 cm^{-1} of M_1-VO_2 have been attributed to A_g phonons, whereas modes at 141, 262, 442, 484, 582, and 821 cm^{-1} belong to B_g symmetry. The signals at 224 and 393 cm^{-1} probably correspond to second-order Raman scattering of the type $A_g + B_g$; i.e., contain contributions of both representations. However, it should be noted that not all the assignments are unequivocal and differ between different works, as pointed out by Shibuya and Sawa.[22] Although some of the Raman signals overlap in our spectrum and cannot be resolved and others may be affected by the TiO_2 signals, the assignment of these additional Raman features to the M_1-phase of VO_2 on the basis of their Raman shifts is unambiguous. The monoclinic M_2-phase of VO_2 possesses the same number of Raman active modes according to group theory. However, the distribution of the character of these modes between A_g and B_g is somewhat different. Group theory yields 10 A_g and 8 B_g modes. More importantly, the experimentally observed Raman shifts and intensities of these modes differ a great deal from those reported for the M_1-phase reflecting the slightly different arrangement of the VO_2 structural units within the two monoclinic unit cells. For example, the distinct peak at 389 cm^{-1} is not present in the M_2 phase, instead, another signal occurs at 435 cm^{-1}. Moreover, the 612 cm^{-1} peak is blue-shifted by about 40 wavenumbers in the M_2-phase.[14,44] Furthermore, Figure S9 shows spectra of $Ti_xV_{1-x}O_2$ thin films of different

x for the same orientation of the substrate and defined parallel and crossed polarization geometries.

In what follows, we discuss the experimental evidence concerning the MIT of the $Ti_xV_{1-x}O_2$ thin films on the (110) TiO_2 substrate. The temperature-dependent resistance curves of three $Ti_xV_{1-x}O_2$ thin films on (110) TiO_2 of different x are shown in Figure 1D. The resistance is measured as a function of sample temperature during heating (red data points) and cooling (blue data points). The resistance curves of all samples exhibit a step-like increase with decreasing temperature (see Figure S7). This step-like jump in resistance corresponds to the MIT. The resistance is low in the metallic phase due to the presence of free-carriers. The free carriers vanish when the VO_2 becomes insulating.[45,46] Thus, the resistance rises abruptly. The temperature where the resistance step occurs is a measure of the phase transition temperature T_c of the MIT (indicated by the dashed vertical lines in the figure). The transition temperature T_c decreases with increasing Ti-content x of the $Ti_xV_{1-x}O_2$ thin films.

Graphs (a) and (b) of Figure 2 show a series of θ-2θ-traces of $Ti_xV_{1-x}O_2$ with x of 2.5% and 5.3%, respectively, as a function of temperature between 30 and 90°C and in the 2θ-range from 55° to 58.5°. Features corresponding to the signals from the $(220)_r$ TiO_2, the R-VO_2 $(220)_r$ as well as the corresponding (022) M_1-VO_2 planes are expected to occur in the series of θ-2θ-traces. Both series of XRD traces exhibit a change of appearance as a function of temperature corresponding to switching from a (022) M_1-VO_2 reflex at higher 2θ-values to the R-VO_2 $(220)_r$ reflex at slightly lower values. However, the structural transition becomes less distinct with increasing x as the reflexes of R and M_1-phase approach each other.

Signatures of the structural phase transition are also observed in a series of Raman spectra taken at different temperatures. As an example, Figure 2C shows a series of Raman spectra of the $Ti_xV_{1-x}O_2$ thin film with $x = 2.5\%$ recorded in the temperature range between 20 and 80°C. With increasing temperature, the modes of the M_1-VO_2 phase decrease in intensity and then disappear and on decreasing the temperature again, the modes of the M_1-phase reappear. The reversible behavior of the intensities of the modes of the M_1-phase on temperature reflects the structural phase transition from the M_1-phase to the R-phase of the $Ti_xV_{1-x}O_2$ thin film. We do not observe any signs of a transformation of the M_1 phase into the M_2 phase. The Raman features of the high-temperature phase of VO_2 are hard to discern but start to appear in some of the samples above T_c (for more details, see discussion of Figure 3). Again, the phase transition occurs in a temperature range rather than abruptly at a specific temperature value, i.e., we extract the corresponding value for the phase transition temperature T_c as the center of this range.

It is worth noting, that, for any specific sample, the temperature range, where signatures of the phase transition occur in a measurement, is about the same for all methods used, i.e., temperature-dependent resistance measurements, Raman spectroscopy, and XRD. Furthermore, in the electrical measurements, we do not observe hints in the corresponding hysteresis loops that are indicative of two-phase transitions taking place, i.e., M_1-M_2-R. The common approach for each type of measurement is to translate the temperature range where the transition takes place into a single value of the phase transition temperature T_c of the sample. However, this is prone to generating uncertainty for several reasons. For example, in inhomogeneous thin films, different parts of the sample volume may pass through the phase transition at somewhat different temperatures. Furthermore, different methods are used to probe the inhomogeneity of the thin film differently. For example, in transmittance measurements of a thin film along the growth direction, the impact of absorbing layers close to the surface is bigger than for layers located deeper inside the film. In contrast, electrical transport measurements probe the formation of a highly conducting percolation path in the film plane. This implies that the approach taken to translate the experimental signature obtained by a certain method in the temperature range of interest into a single T_c-value is specific to the method. In the case of the electrical measurements, we define T_c by determining the temperature values corresponding to the minima of the first derivatives of the decimal logarithm of the resistance curves with respect to the temperature measured during heating and cooling and taking their average value.[21] A T_c-value is extracted from the temperature-dependent Raman spectra by extrapolating the dependence of the Raman intensity of the modes on temperature to zero intensity and taking the intersection point with the abscissae as T_c-value. In the case of the XRD measurements, we take the center of the temperature range where the XRD reflexes of both phases are visible as T_c-value. Obviously, the narrower the temperature range where the transition occurs, the smaller the difference between the T_c values determined by the different approaches.

Figure 2D compares the T_c-values derived from specific experimental signatures obtained by the three methods. The three dependencies of T_c on Ti-content x reveal a clear trend that is independent of the method used for probing the phase transition, i.e., the $Ti_xV_{1-x}O_2$ thin films on (110) TiO_2 show a reduction of T_c with increasing x. All the thin film samples undergo a structural phase transition from the monoclinic M_1-phase to the rutile phase with increasing temperature without passing the intermediate monoclinic M_2-phase. These findings differ from those known for stoichiometric crystalline $Ti_xV_{1-x}O_2$ bulk material. The difference is caused

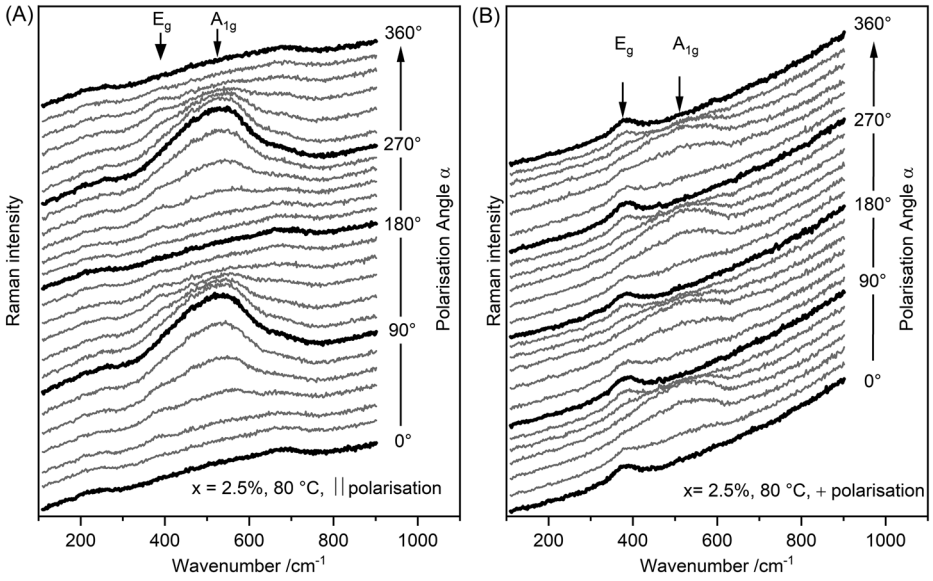

FIGURE 3 Angle-dependent Raman spectra of a $Ti_xV_{1-x}O_2$ thin film with $x = 2.5\%$ taken at $T = 80°C > T_c$ for (A) parallel and (B) crossed polarization geometry.

by unintentional doping by oxygen vacancies due to energetically driven migration of the vacancies from the substrate into the thin film.[20,21] In addition, the reduction of lattice strain with increasing x also contributes to the decreasing trend of T_c with x. Both effects together are seemingly stronger than the expected increase of T_c due to the alloying itself.[38]

We will now analyze the polarization and angle dependence of the Raman signals of the $Ti_xV_{1-x}O_2$ thin films and the TiO_2 substrate at room temperature (below T_c) and at 80°C (above T_c) to further assess the structural properties of the low-temperature and the high-temperature phase of the thin films. In particular, we will clarify the epitaxial relationship between the lattices of the low and high-temperature phase of the $Ti_xV_{1-x}O_2$ films and that of the TiO_2 substrate. We also employed XRD phi scans to determine the epitaxial relationship, see Figure S8.

For this purpose, we use the Cartesian coordinates (x,y,z) of the rutile TiO_2 substrate as a reference frame. The rutile z-axis lies in the plane of the (110) substrate. In the backscattering geometry used, the directions of incoming light and the Raman scattered light are parallel to the rutile $[110]_r$ direction and the linear polarizations lie in the $(110)_r$ plane. We denote the angle between the linear polarization of the incoming laser light and the rutile z-axis by α. The angle α is varied in the angle-dependent Raman measurements. Such angle-dependent measurements have been performed detecting the Raman scattered light either with a polarization parallel or perpendicular to that of the incoming laser. Taking the known Raman tensors $\mathcal{R}$ of the rutile structure (e.g., from Ref. 47) yields the Raman intensities of modes belonging to the four irreducible representations according to

$$I(\alpha) \propto \left| \vec{e}_{\mathrm{det}}^{\,T}(\alpha) \cdot \mathcal{R} \cdot \vec{e}_{\mathrm{exc}}(\alpha) \right|^2 \quad (4)$$

where $\vec{e}_{\mathrm{det}}^{\,T}(\alpha)$ and $\vec{e}_{\mathrm{exc}}(\alpha)$ denote the normal vectors along the polarization directions of the detected scattered light and the incoming excitation laser light, respectively. The angle dependences obtained are given in Table 2 for parallel and crossed polarizations of the incoming laser and the backscattered Raman light. Details of the derivation are given in the Supporting Information. Furthermore, Figures S2 and S3 demonstrate that the intensities of the Raman modes of the TiO_2 substrate obey the derived angle dependence. In particular, we have used the angle-dependence $I^{\parallel}_{B_{2g}}(\alpha) \propto d^2 \cdot \sin^4\alpha$ of the B_{2g} mode of rutile TiO_2 at 826 cm^{-1}, which exhibits a 180° periodicity for parallel polarizations, to pin down the orientation of the c-axis ($\pm z$-direction) in the plane of the (110) TiO_2 substrate for each sample. The corresponding measurements were performed on the backside of the substrate. The reason is that signals originating from the film and the substrate may overlap in spectra taken of the front surface, where the $Ti_xV_{1-x}O_2$ thin film is deposited. In what follows all angles α labeling the series of angle-dependent Raman spectra of the $Ti_xV_{1-x}O_2$ layers are given with respect to the orientation of the c-axis of the substrate. Unfortunately, we cannot distinguish between [001] and $[00\bar{1}]$ directions using this approach.

Figure 3 shows two series of Raman spectra of a $Ti_xV_{1-x}O_2$ thin film with $x = 2.5\%$ as a function of the angle α taken at 80°C. This thin film is thick enough that no or only very weak signals of (110) TiO_2 substrate are observable in the measurements at $T > T_c$. The c-axis of the (110) TiO_2 substrate was determined by corresponding angle-dependent Raman measurements at $T < T_c$ on

TABLE 2 Angle dependence of the Raman intensity of modes of different irreducible representations for backscattering experiments on the (110) plane of a rutile crystal for linearly polarized excitation laser light and detection of the backscattered Raman signal in parallel and crossed polarization configurations. The angle α denotes the angle between the rutile z-direction and the incoming polarization, the parameters *a*, *b*, *c*, and *d* denote tensor matrix elements.

	Parallel polarizations	Crossed polarizations
$\mathbf{A_{1g}}$	$I^{\parallel}_{A_{1g}}(\alpha) \propto a^2 \cdot \sin^4\alpha + 2ab \cdot \sin^2\alpha \cdot \cos^2\alpha + b^2 \cdot \cos^4\alpha$	$I^{\times}_{A_{1g}}(\alpha) \propto (a^2 - 2ab + b^2) \cdot \sin^2 2\alpha$
$\mathbf{B_{1g}}$	$I^{\parallel}_{B_{1g}}(\alpha) \propto c^2 \cdot \sin^4\alpha$	$I^{\times}_{B_{1g}}(\alpha) \propto \frac{1}{4}c^2 \cdot \sin^2 2\alpha$
$\mathbf{B_{2g}}$	$I^{\parallel}_{B_{2g}}(\alpha) \propto d^2 \cdot \sin^4\alpha$	$I^{\times}_{B_{2g}}(\alpha) \propto \frac{1}{4}d^2 \cdot \sin^2 2\alpha$
$\mathbf{E_g}$	$I^{\parallel}_{E_g}(\alpha) \propto e^2 \cdot \sin^2 2\alpha$	$I^{\times}_{E_g}(\alpha) \propto e^2 \cdot \cos^2 2\alpha$

the back surface of the (110) TiO_2 substrate as described above. The left and right graphs of Figure 3 correspond to measurements in parallel and crossed polarization geometry, respectively. There is only one previous report by Schilbe on the R-VO_2 Raman spectrum.[48] He studied a VO_2 single crystal and was able to identify four broad Raman signals (i.e., line width of about 100 cm^{-1}) at 240, 390, 510, and 625 cm^{-1}. Assuming a correspondence to the four Raman signals of structurally equivalent rutile TiO_2 modes, he assigned the irreducible representations B_{1g}, E_g, A_{1g}, and B_{2g} to the Raman signals at 240, 390, 510, and 625 cm^{-1}, respectively. In both series of angle-dependent Raman spectra of the high-temperature phase of the $Ti_{0.025}V_{0.975}O_2$ thin film, we observe two clear signals, a strong mode at 520 cm^{-1} and a weaker mode at 390 cm^{-1}, which somewhat overlaps with the mode at 520 cm^{-1} and is better visible for crossed polarizations. Both modes exhibit a distinct angle dependence in both polarizations. The Raman features reported by Schilbe at about 240 cm^{-1} and 625 cm^{-1} are also discernable, but due to the strong background too weak to unambiguously discuss the angle dependence of their intensity. Figure 4 shows the angle dependence of the mode intensities of both strong modes for both polarization geometries together with curves fitted to the anticipated angle dependences for the rutile structure according to Table 2, i.e, those corresponding to A_{1g} symmetry in case of the 520 cm^{-1} mode and those corresponding to E_g symmetry in case of the 390 cm^{-1} mode. Three conclusions can be drawn. First, the assignment of the irreducible representations to these two modes by Schilbe is correct. Second, the high-temperature phase of our $Ti_xV_{1-x}O_2$ thin films is indeed the rutile phase. And, third, the unit cell of the rutile $Ti_xV_{1-x}O_2$ thin film grows pseudomorphically on top of the (110) rutile TiO_2 substrate, i.e., can be described by the same coordinate system (*x*,*y*,*z*) as the crystalline TiO_2 substrate.

Figure 5 depicts the two series of angle-dependent Raman spectra for parallel and crossed polarization geometry of the $Ti_xV_{1-x}O_2$ thin film with $x = 2.5\%$ in its low-temperature M_1 phase. As pointed out above, the identification of $\alpha = 0°$ (or 180°) based on the angle dependence of TiO_2 Raman peaks allows us to align the angle dependence of the M_1-Raman signals of the $Ti_xV_{1-x}O_2$ thin film with respect to the orientation of the *c*-axis of the rutile TiO_2 substrate. From the analysis of Figures 4 and S3, we know the epitaxial relationship between $Ti_xV_{1-x}O_2$ thin film in the rutile high-temperature phase and crystalline substrate. Moreover, we can assume in the derivation of the angle dependence of the Raman modes of the A_g and B_g irreducible representations of the M_1-phase that the relationships between the Cartesian coordinate systems of the unit cells of the M_1-phase of the thin film and the rutile TiO_2 substrate (equivalent to that of the R-phase of the thin film) follow the transformations described in Equations (1) to (3) established for bulk crystals. This yields the following equation for deriving the angle dependence of the Raman modes of the 180°-domains of the M_1-phase of a $Ti_xV_{1-x}O_2$ thin film as a function of the rotation angle α as defined above:

$$I(\alpha) \propto \left| \vec{e}^{\,T}_{det}(\alpha) \cdot \Im_i^{-1} \cdot \mathcal{R}' \cdot \Im_i \cdot \vec{e}_{exc}(\alpha) \right|^2 \qquad (5)$$

where $\Im_i$ denotes the transformation matrix given by Equation (3) and $\mathcal{R}'$ denotes the Raman tensor of an irreducible representation of the monoclinic crystal system (e.g., given in Ref. 47). The characteristic angle dependences for modes corresponding to the A_g and B_g irreducible representations are given in Table 3 for the two types of domains. Details of the derivation of the formulas can be found in the Supporting Information.

The verification of this requirement is straightforward by looking at the temperature-dependent Raman data in Figure 2C, which clearly shows the Raman modes of the M_1-phase, which are only weakly affected by the substrate modes. We will analyze in detail the modes of the M_1-phase observed at 141 cm^{-1}, 194 cm^{-1}, 262 cm^{-1},

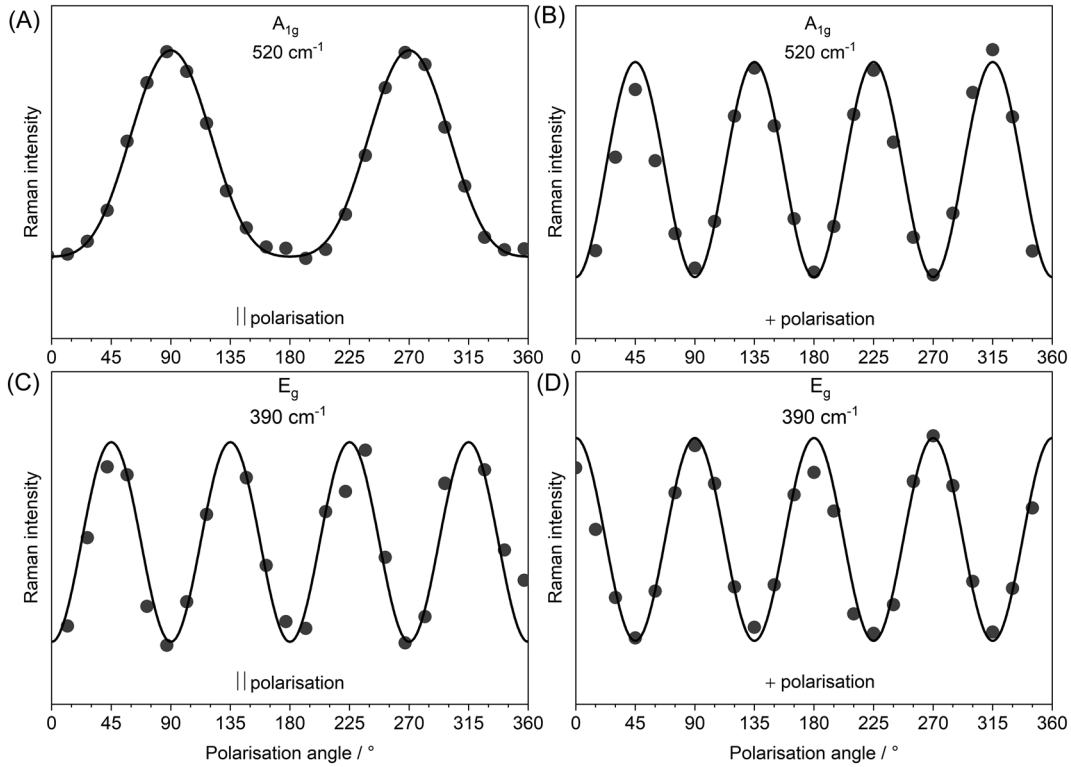

FIGURE 4 Angle dependence of the intensities of the E_g and the A_{1g} mode at 390 cm^{-1} and 520 cm^{-1}, respectively, of rutile $Ti_xV_{1-x}O_2$ thin film with $x = 2.5\%$ for parallel and crossed polarization geometry. The mode intensities are background corrected and fitted to the anticipated angle dependences for a rutile crystal phase according to Table 2. Symbols represent the experimental data and solid lines are the fitted curves.

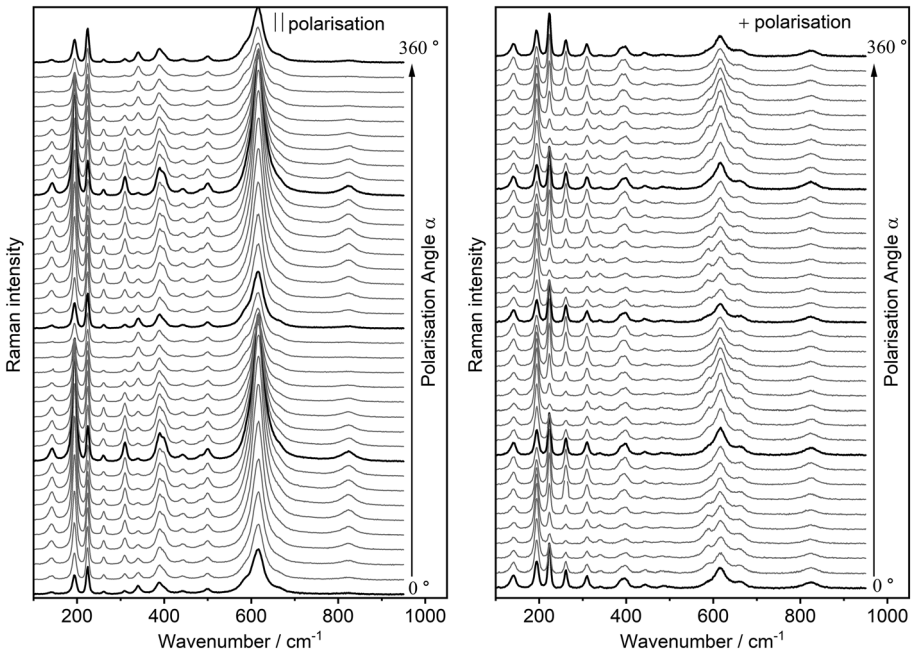

FIGURE 5 Angle-dependent Raman spectra of a $Ti_xV_{1-x}O_2$ thin film with $x = 2.5\%$ taken at room temperature ($T < T_c$) for (a) parallel and (b) crossed polarization geometry. The thicker lines correspond to spectra taken at $\alpha = 0°$ (360°), 90°, 180°, and 270°.

310 cm^{-1}, 340 cm^{-1}, and 443 cm^{-1}, which correspond to one-phonon Raman scattering. We will also consider the signal at 224 cm^{-1}, which should correspond to a two-phonon Raman process and contain contributions $A_g + B_g$.

Figure 6 shows the angle dependence of the intensity of three B_g modes for the parallel and crossed

polarization geometry and samples of different x. These are the modes at about 141 cm^{-1}, 260 cm^{-1}, and 443 cm^{-1}. First, it is important to note that the expressions for $I_{Bg}^{\|i}(\alpha)$ for $i=1,2$ can be expressed as a sum of higher powers of $\sin^2\alpha$ (making use of the identity $\sin^2\alpha = 1-\cos 2\alpha$) and $\sin 2\alpha$. Accordingly, it holds $I_{Bg}^{\|i}(\alpha=0)=0$ for both domains in this polarization configuration. It can be seen that the Raman intensity of all three B_g modes fulfills this condition at $\alpha=0$ for all x. The angular dependences of all three modes in parallel polarization geometry possess a 180°-periodicity whereas in crossed polarization geometry a 90°-periodicity is observed. Nevertheless, the angle dependence of the three B_g modes shown differs considerably. The mode at 141 cm^{-1} shows a single peak structure whereas that at 260 cm^{-1} exhibits a double-peak structure, which is repeated every 180°. The mode at 443 cm^{-1} shows an intermediate behavior, i.e., for some x the double peak structure for others the single peak structure. The situation is slightly different in crossed polarization geometry. The modes at 260 cm^{-1} and 443 cm^{-1} exhibit maximal mode intensity at $\alpha=0$ whereas the angular dependence of the mode at 141 cm^{-1} possesses a maximum at $\alpha=0$ in case of the two low-x samples, but a minimum for the samples with other x. This is at first somewhat surprising but arises simply due to different ratios $e:f$ of the tensor matrix elements e and f or slight variations in the proportions of domains of type 1 and 2 within the laser spot as we will see below. The angle dependences of all B_g modes studied vary only little with the Ti-content x of the $Ti_xV_{1-x}O_2$ thin films, indicating that the variation of the tensor elements e and f with Ti-content x is rather small in the range between 0% and 8.6%.

Figure 7 depicts similar plots of the Raman intensities of three A_g modes of the $Ti_xV_{1-x}O_2$ thin films as a function of x for both polarization geometries. It should be noted that the intensity of an A_g mode does not need to go to zero between 0 and 360 cm^{-1}. The angular dependence of the intensity of three modes in parallel polarization also possesses a 180°-symmetry. The same holds for the perpendicular polarization geometry, but with a dominant 90°-periodic component. The maxima of the angular intensity dependence for parallel polarization are approximately 90° for the modes at 193 cm^{-1} and 310 cm^{-1} whereas the maximum is at 0° for the mode at 340 cm^{-1}. Furthermore, the mode at 310 cm^{-1} shows a 180°-periodic double peak structure whereas the other two modes exhibit a 180°-periodic single peak. In crossed polarization configuration, the angle dependence of the intensity of the mode at 310 cm^{-1} shows maxima at 0° (360°), 90°, 180°, and 270° whereas those of the other two modes exhibit minima at these angles. These differences are caused by the different correlations between the tensor elements a, b, c, and d of the Raman tensors of the three modes as shown below. Moreover, as for the B_g modes, only slight variations occur as a function of Ti content x.

In what follows, we will analyze the angular dependence of the intensities of the six Raman modes based on the expressions given in Table 3 for the two types of 180°-domains. The expressions in the table reveal that the angular dependences of a mode are different for the two types of 180°-domains (see also top graphs of Figures S4 and S5). Indeed, we find for all six modes that the dependence of their Raman intensity on angle α can neither be fitted by the equations for type 1 nor those for type 2 domains. Therefore, we believe that the angular dependences derived for the mode intensities depend strongly on portions λ and (1 – λ) of the two types of domains within the laser spot (see also lower graphs of Figures S4 and S5). To further corroborate our assumption, we have fitted the angle dependence of the Raman intensities of the B_g and A_g modes in Figures 6 and 7 for every sample by the following functions:

$$\begin{aligned} I_{B_g}^{\|tot}(\alpha) &= \lambda\cdot I_{B_g}^{\|1}(\alpha) + (1-\lambda)\cdot I_{B_g}^{\|2}(\alpha) \\ I_{B_g}^{\times tot}(\alpha) &= \mu\left[\lambda\cdot I_{B_g}^{\times 1}(\alpha) + (1-\lambda)\cdot I_{B_g}^{\times 2}(\alpha)\right] \\ I_{A_g}^{\|tot}(\alpha) &= \lambda\cdot I_{A_g}^{\|1}(\alpha) + (1-\lambda)\cdot I_{A_g}^{\|2}(\alpha) \\ I_{A_g}^{\times tot}(\alpha) &= \mu\left[\lambda\cdot I_{A_g}^{\times 1}(\alpha) + (1-\lambda)\cdot I_{A_g}^{\times 2}(\alpha)\right] \end{aligned}, \qquad (6)$$

where λ and $(1-\lambda)$ denote the proportions of the domain 1 and 2, respectively, within the volume probed by the laser spot. These proportions should be the same for all modes of the same sample. The tensor elements of a particular mode must be the same for parallel and crossed polarization geometry but may differ for different modes even if they are of the same representation, i.e., the three B_g or the three A_g modes studied. The factor μ accounts for slight differences in the sensitivity of the Raman system between the parallel and the crossed polarization geometry and is used as a free parameter. We find $\mu \cong 1 \mp 0.1$ for spectra taken on the same sample spot, as expected. The fit results are shown as solid lines in Figures 6 and 7 and confirm that indeed both types of domains must be present in the thin films at room temperature. In the Supporting Information, we also show that the angle dependence of A_g and B_g modes is indeed sensitive to the portions λ and (1-λ) of the two types of domains within the laser spot.

For all samples, the values of λ lie in the range between 0.45 and 0.55. This suggests, first, that the domains must be much smaller than the laser spot size and, second, both types of domains form with the same

TABLE 3 Angle dependence of the Raman intensity of modes of different irreducible representations for backscattering experiments $Ti_xV_{1-x}O_2$ thin films in the M_1-phase on (110) rutile TiO_2 substrates for linearly polarized excitation laser light and detection of the backscattered Raman signal in parallel and crossed polarization configurations. The angle α denotes the angle between the rutile z-direction of the TiO_2 substrate and the incoming polarization, and the parameters *a*, *b*, *c*, *d*, *e*, and *f* denote tensor matrix elements. The superscripts 1 and 2 stand for domains of type 1 and 2, respectively. The results are in agreement with those by Shibuya and Sawa.[22]

	Parallel polarizations	Crossed polarizations
$\mathbf{A_g}$	$I^{\parallel 1}_{A_g}(\alpha) \propto \left\lvert \frac{1}{4}(2a+b+c)+\frac{1}{4}(2a-b-c)\cdot\cos 2\alpha+\frac{d}{\sqrt{2}}\cdot\sin 2\alpha \right\rvert^2_2$ $I^{\parallel 2}_{A_g}(\alpha) \propto \left\lvert \frac{1}{4}(2a+b+c)+\frac{1}{4}(2a-b-c)\cdot\cos 2\alpha-\frac{d}{\sqrt{2}}\cdot\sin 2\alpha \right\rvert^2_2$	$I^{\times 1}_{A_g}(\alpha) \propto \left\lvert \frac{1}{4}(b+c-2a)\cdot\sin^2 2\alpha+\frac{d}{\sqrt{2}}\cdot cos2\alpha \right\rvert^2_2$ $I^{\times 2}_{A_g}(\alpha) \propto \left\lvert \frac{1}{4}(b+c-2a)\cdot\sin^2 2\alpha-\frac{d}{\sqrt{2}}\cdot cos2\alpha \right\rvert^2_2$
$\mathbf{B_g}$	$I^{\parallel 1}_{B_g}(\alpha) \propto \left\lvert \frac{f}{2}\cdot(1-\cos 2\alpha)+\frac{e}{\sqrt{2}}\cdot\sin 2\alpha \right\rvert^2_2$ $I^{\parallel 2}_{B_g}(\alpha) \propto \left\lvert \frac{f}{2}\cdot(1-\cos 2\alpha)-\frac{e}{\sqrt{2}}\cdot\sin 2\alpha \right\rvert^2_2$	$I^{\times 1}_{B_g}(\alpha) \propto \left\lvert \frac{f}{2}\cdot\sin 2\alpha+\frac{e}{\sqrt{2}}\cdot\cos 2\alpha \right\rvert^2_2$ $I^{\times 2}_{B_g}(\alpha) \propto \left\lvert \frac{f}{2}\cdot\sin 2\alpha-\frac{e}{\sqrt{2}}\cdot\cos 2\alpha \right\rvert^2_2$

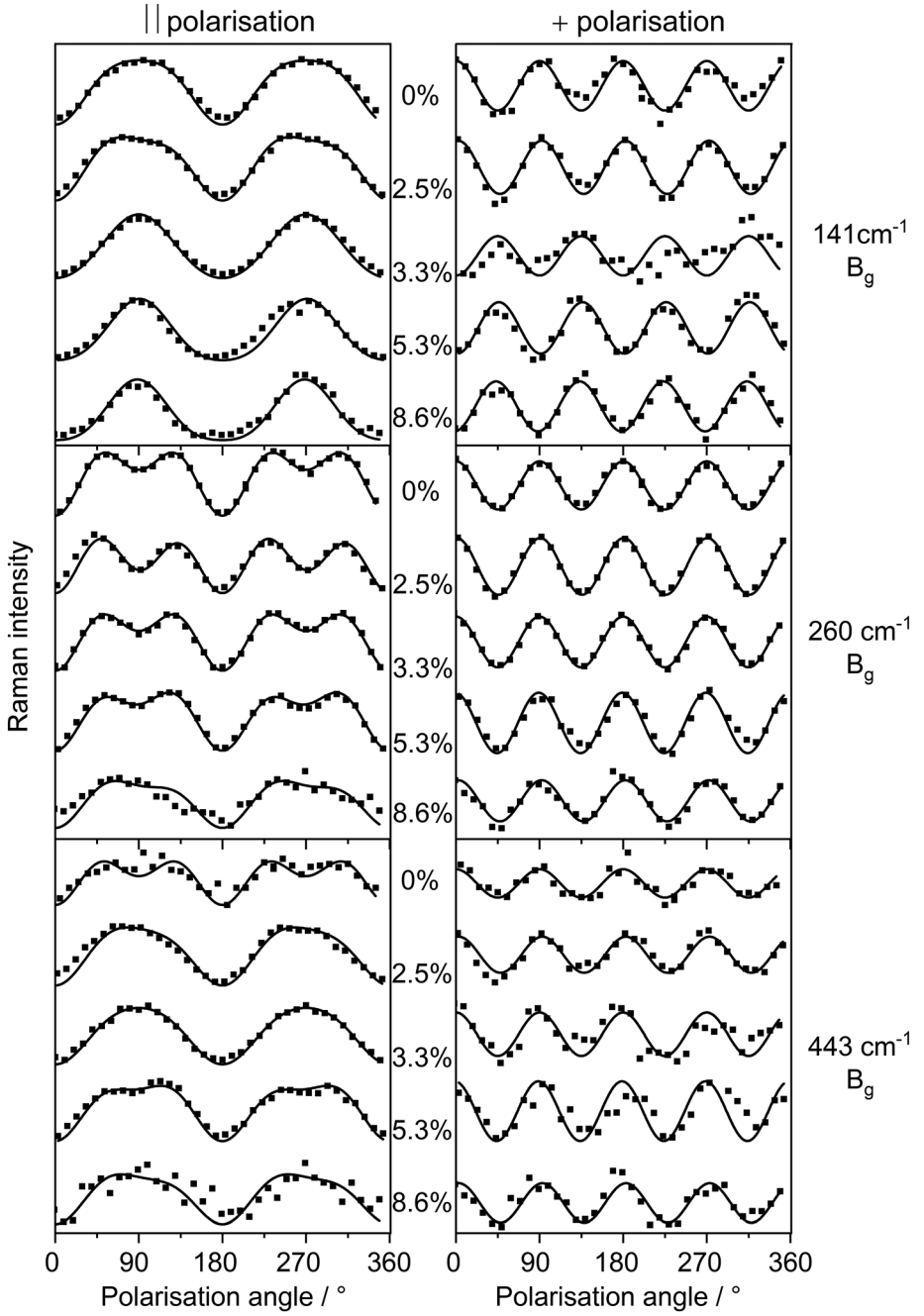

FIGURE 6 Angle-dependence of the Raman intensity of three B_g modes of the M_1-phase of $Ti_xV_{1-x}O_2$ thin films on (110) rutile TiO_2 substrates for parallel (left) and crossed polarization geometry (right). Samples of $x = 0\%$, 2.5%, 5.3%, and 8.6% were studied. The results of the B_g modes at 141 cm^{-1}, 260 cm^{-1}, and 443 cm^{-1} are shown from top to bottom. Symbols represent experimental data and solid lines fitted curves according to Equation (6).

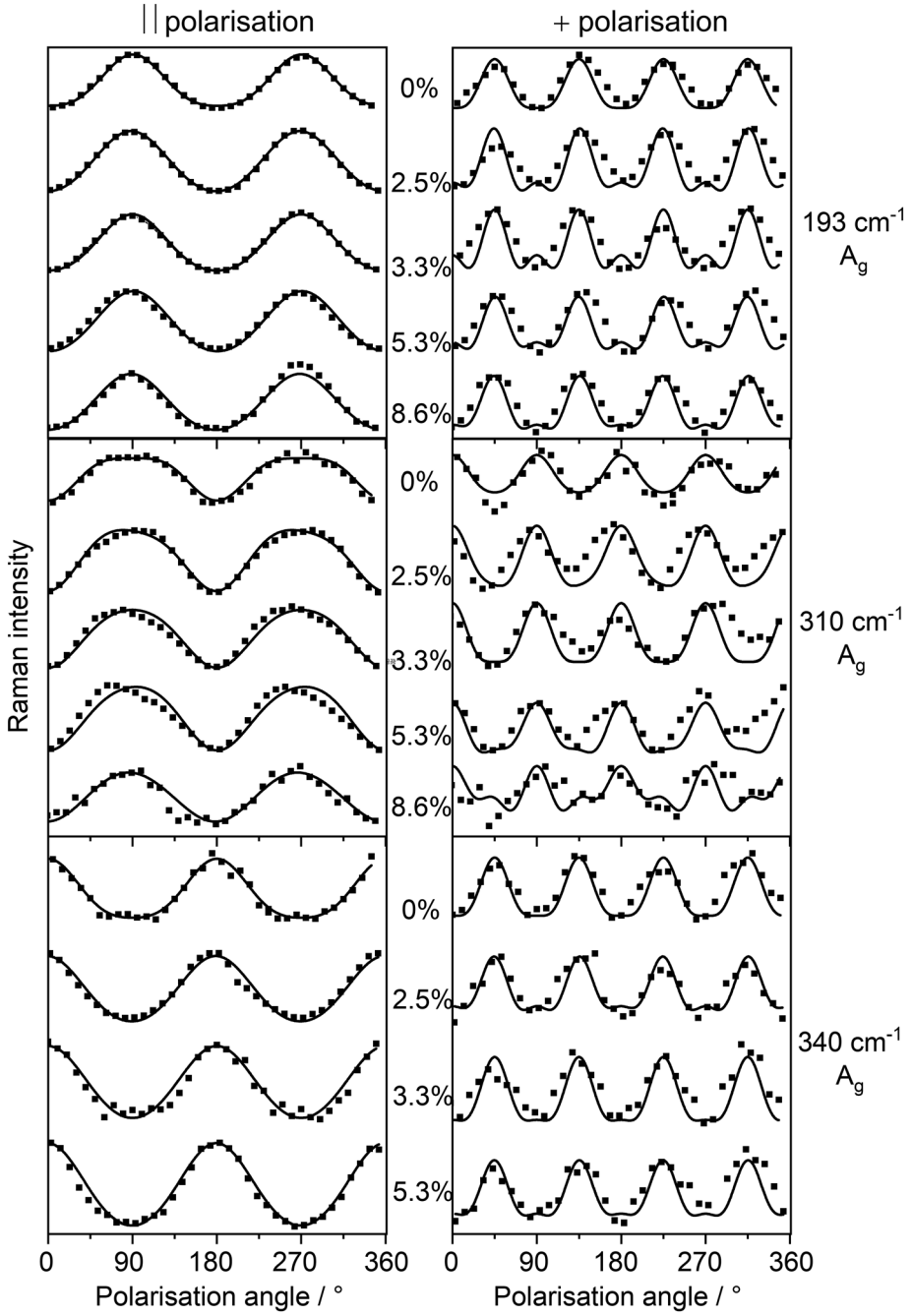

FIGURE 7 Angle-dependence of the Raman intensity of three prominent A_g modes of the M_1-phase of $Ti_xV_{1-x}O_2$ thin films on (110) rutile TiO_2 substrates for parallel (left) and crossed polarization geometry (right). Samples of x = 0%, 2.5%, 5.3%, and 8.6% were studied. The results for the A_g modes at 193 cm^{-1}, 310 cm^{-1}, and 340 cm^{-1} are shown from top to bottom of the figure. Symbols represent experimental data and solid lines fitted curves according to Equation (6). It should be noted that the A_g modes do not go to zero, i.e., in the graphs we emphasize the variation of the Raman intensity with rotation angle in order to highlight the evolution with Ti-content *x*. All curves were fitted according to Equation (6).

likelihood when cooling down the thin film after completing the deposition process. We also find that the correlations between the Raman tensor elements differ for different Raman modes of the same representation. These differences are larger than the variation of the tensor elements for the same Raman mode as a function of *x* as can be seen in Table 4. In other words, the incorporation of Ti only weakly affects the displacement pattern and the bonding between the atoms involved in a particular lattice vibration. The normalized tensor elements that we have determined for binary VO_2 on (110) TiO_2 are in good agreement with those obtained by Shibuya and Sawa for VO_2 on (110) MgF_2, in particular, when considering the differences in the substrate (110) MgF_2 vs (110) TiO_2 and in excitation laser wavelength 539 nm vs 515 nm. The values derived for the fitting parameters f/e or $A = 2{\cdot}a$, $B = b + c$, and $D = \sqrt{2}{\cdot}d$ for the B_g and A_g discussed using the normalized tensor elements of Shibuya and Sawa are given in brackets in Table 4.

It is worth mentioning that the angle dependences of the intensity of the mode at 224 cm^{-1} (not shown) exhibit 90°-periodicity in both parallel and crossed polarization configurations. These angle dependences cannot be

TABLE 4 Correlations between the tensor elements e and f of the B_g modes at 141 cm^{-1} 260 cm^{-1}, and 443 cm^{-1} for different x. The same for the correlations of the tensor elements a, b, c, and d of the A_g modes at 193 cm^{-1}, 310 cm^{-1}, and 340 cm^{-1}. We define $A = 2 \cdot a$, $B = b + c$, and $D = \sqrt{2} \cdot d$. The parameter λ denotes the portion of domains of type 1 within the laser spot, correspondingly $(1 - \lambda)$ denotes the portion of domains of type 2.

		0% Ti	2.5% Ti	3.3% Ti	5.3% Ti	8.6% Ti
	λ	0.5	0.53	0.5	0.48	0.54
B_g 141 cm^{-1}	f/e	1.09 (1.2)[22]	1.06	1.65	2.16	2.60
B_g 260 cm^{-1}	f/e	0.61 (0.50)[22]	0.50	0.66	0.74	0.88
B_g 443 cm^{-1}	f/e	0.64 (0.57)[22]	1.02	1.17	0.90	0.99
A_g 193 cm^{-1}	$A: B: D$	0.2: 1: 0.25(0.37: 1: 0.18)[22]	0.36: 1: 0.43	0.37: 1: 1.10	0.35: 1: 0.45	0.37: 1: 0.32
A_g 310 cm^{-1}	$A: B: D$	0.32: 1: 1.16(0.2: 1: 0.51)[22]	0.32: 1: 1.03	0.38: 1: 0.86	0.31: 1: 0.92	0.57: 1: 0.51
A_g 340 cm^{-1}	$A: B: D$	6.49: 1: 1.33 (3.7: 1: 0.21)[22]	2.4: 1: 0.84	1.62: 1: 0.27	2.15: 1: 0.6	not discernable in the spectrum

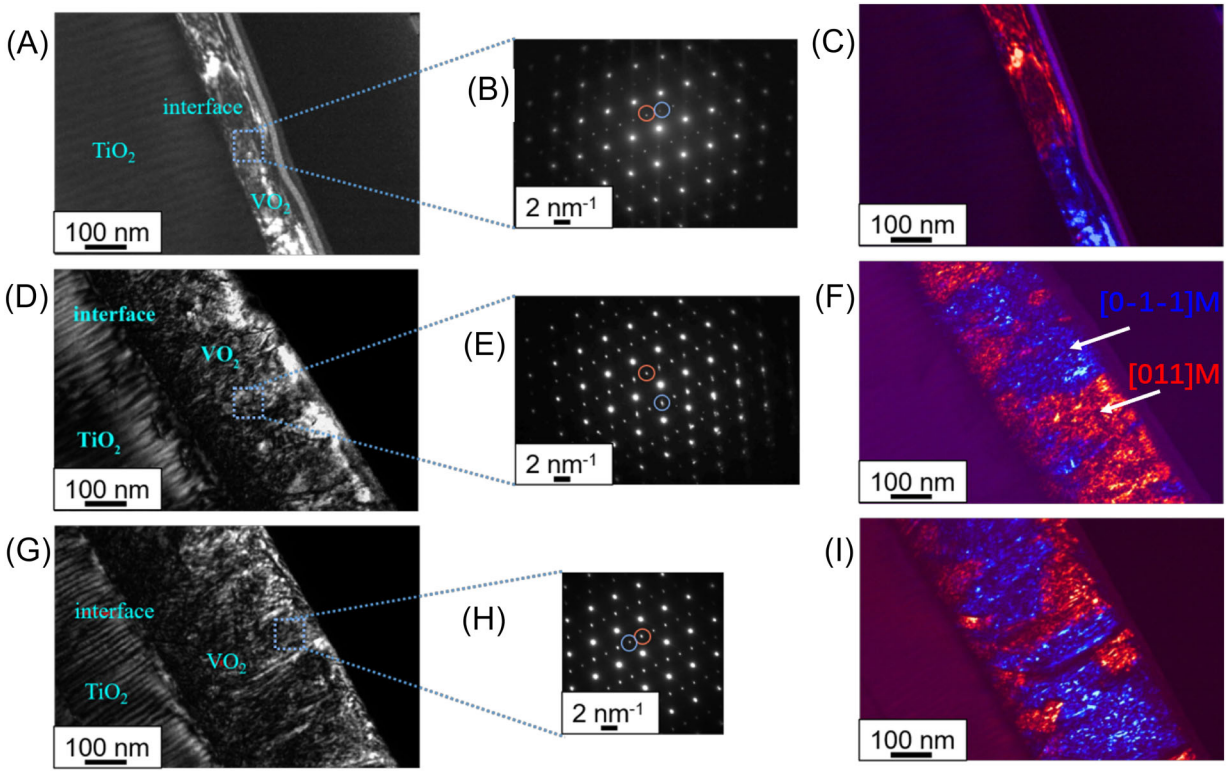

FIGURE 8 Results of transmission electron microscopic studies of an undoped VO_2 thin film (A–C), a $Ti_xV_{1-x}O_2$ thin film doped with x = 4.7% (D–F), and a $Ti_xV_{1-x}O_2$ thin film doped with x = 8.6% (H–I). The transmission electron microscope images of cross-sectional areas of the three samples are shown on the left, corresponding diffraction patterns taken in the areas indicated are shown in the center, and the corresponding dark field images on the right. The dark field images confirm the formation of 180° domains. The two types of domains are color-coded in the dark-field images by red and blue indicating domain dimensions in the order of 100 nm.

satisfactorily fitted by the equations given in Equation (6) for an A_g or a B_g mode alone. However, they can be fitted by the sum of the equations for an A_g and a B_g mode, i.e., can be described by a representation that contains both irreducible representations. This feature is typical for second-order Raman scattering where modes of opposite

k-vector contribute. Overall, our findings for the modes in the M_1 phase, which we have studied in detail are in perfect agreement with the assignment by Shibuya and Sawa.[22]

To further corroborate the 180°-domain formation, we performed a careful transmission electron microscopic study of three $Ti_xV_{1-x}O_2$ thin films in the low-temperature M_1-phase. The results are presented in Figure 8 in graphs (A) to (C), in (D) to (F), and (G) to (I) for the undoped thin film with $x = 0\%$, that with $x = 4.7\%$, and that with $x = 8.6\%$, respectively. TEM cross-sectional views of the three samples are depicted on the left of the figure in graphs (A), (D), and (G). In the middle, the corresponding diffraction patterns are shown in (B), (E), and (H). Darkfield images that are assigned to the diffraction spots indicated in the diffraction patterns are depicted on the right. The dark field images of all three samples reveal two domain orientations that can be assigned to a monoclinic M_1-phase of the thin films and exhibit a mirror symmetry (180°). The areas color-coded in red and blue show $[011]_m$ and $[0\text{–}1\text{-}1]_m$ orientations that are randomly distributed over the entire thin film volume, i.e., the results are in excellent agreement with the interpretation of Raman data in Figures 6 and 7. These findings also agree with similar TEM measurements performed on comparable VO_2 thin films by Zheng et al.[30]

4 | CONCLUSIONS

We have determined the crystalline phases of $Ti_xV_{1-x}O_2$ thin films on (110) rutile TiO_2 substrates, which are involved in the structural phase transition accompanying the MIT for x up to 8.6%. For all x, the low-temperature insulating phase is the monoclinic M_1-phase and the high-temperature metallic phase is the rutile phase as in donor-doped VO_2 bulk material. We do not observe any sign of an intermediate M_2 phase. This behavior differs from that of stoichiometric crystalline $Ti_xV_{1-x}O_2$ bulk material. It is explained by the formation of oxygen vacancies in $Ti_xV_{1-x}O_2$ thin films triggered by the TiO_2 substrate. The n-type doping by the vacancies predominantly determines the behavior of the MIT of the films and counteracts the anticipated effects due to substrate-induced strain in thin films and alloying with Ti. Furthermore, we demonstrate that carefully conducted Raman spectroscopic studies are a powerful tool for determining the epitaxial relationships of the low-temperature and the high-temperature phase of the deposited $Ti_xV_{1-x}O_2$ thin films and the TiO_2 substrate. We confirm the characteristic Raman spectrum of rutile VO_2 reported by Schilbe for single crystals and prove that his assignment of the four Raman modes to the irreducible representations of tetragonal symmetry is correct. A careful analysis of a series of angle and polarization-dependent Raman spectra of the Raman modes of the M_1-phase clearly shows that 180°-domains of the M_1-phase are formed, each with a defined relationship to the rutile lattice. Both types of domains occur with roughly the same probability. Furthermore, the analysis confirms the assignment of the M_1 modes reported by Shibuya and Sawa to the irreducible representations for monoclinic symmetry. In addition, we find that the identity of a specific vibrational mode reflected by its Raman tensor elements is only weakly affected by the incorporation of Ti into VO_2. The impact of Ti incorporation on the tensor elements of a specific vibration is observed to be marginal in comparison to the variations among the tensor elements of vibrations sharing the same irreducible representation at a constant x. All these findings are in excellent agreement with corresponding TEM and XRD analyses. We conclude that the capability of Raman spectroscopy for providing deeper structural information about this layered system of binary oxides is tremendous and in some cases comparable or even exceeding the capability of a standard XRD analysis. The strong effect that the presence of surrounding layers may have on the properties of VO_2-based layers in device structures, requires thorough investigations of the alteration of the layer's properties. Such information is essential for understanding the underlying microscopic processes and thus for optimizing the device operation. This study underlines that Raman spectroscopy as a non-invasive technique is a suitable tool for this purpose. As a non-invasive tool, it has the potential to be employed during or after the growth of the layered structures employed in the device, during the process of device fabrication as well as during device operation. This way, it will offer valuable insights about device structures.

ACKNOWLEDGEMENTS

This work was supported by the National Natural Science Foundation of China (Grant Nos. 51572073, 11975093, and 62274057), the Sino-German Mobility Program (Grant No. M-0764), the Natural Science Foundation of Hubei Province (Grant Nos. 2019CFA006, 2021EHB005, and 2022EHB023), the Program for Science and Technology Innovation Team in Colleges of Hubei Province (Grant No. T201901), and the China Scholarship Council (award to Hao Lu for 3 year's study abroad at the University of Giessen). Furthermore, we acknowledge the support from the German BMBF (Grant No. 03VP09691), the Austrian Innovation Fund (with Project No. €OAW 4023 Innovation funds), and DFG research grant 510965362. Open Access funding enabled and organized by Projekt DEAL.

ORCID

Hao Lu https://orcid.org/0000-0001-8882-7974

REFERENCES

[1] S. C. Dixon, D. O. Scanlon, C. J. Carmalt, I. P. Parkin, *J. Mater. Chem. C* **2016**, *4*, 6946.
[2] S. Lany, *J. Phys. Condens. Matter* **2015**, *27*, 283203.
[3] B. K. Meyer, A. Polity, D. Reppin, M. Becker, P. Hering, P. J. Klar, T. Sander, C. Reindl, J. Benz, M. Eickhoff, C. Heiliger, M. Heinemann, J. Bläsing, A. Krost, S. Shokovets, C. Müller, C. Ronning, *Phys. Status Solidi B* **2012**, *249*, 1487.
[4] M. Brahlek, L. Zhang, J. Lapano, H.-T. Zhang, R. Engel-Herbert, N. Shukla, S. Datta, H. Paik, D. G. Schlom, *MRS Commun.* **2017**, *7*, 27.
[5] E. Morosan, D. Natelson, A. H. Nevidomskyy, Q. Si, *Adv. Mater.* **2012**, *24*, 4896.
[6] Y. Ke, S. Wang, G. Liu, M. Li, T. J. White, Y. Long, *Small* **2018**, *14*, e1802025.
[7] B. Eifert, M. Becker, C. T. Reindl, M. Giar, L. Zheng, A. Polity, Y. He, C. Heiliger, P. J. Klar, *Phys. Rev. Materials* **2017**, *1*, 014602.
[8] M. Becker, J. Kessler, F. Kuhl, S. L. Benz, L. Chen, A. Polity, P. J. Klar, S. Chatterjee, *Phys. Status Solidi a* **2022**, *219*, 2100828.
[9] P. Shvets, A. Krylov, K. Maksimova, A. Goikhman, *J. Raman Spectrosc.* **2024**, *55*, 445.
[10] P. Shvets, O. Dikaya, K. Maksimova, A. Goikhman, *J. Raman Spectrosc.* **2019**, *50*, 1226.
[11] C. Wu, F. Feng, Y. Xie, *Chem. Soc. Rev.* **2013**, *42*, 5157.
[12] Z. Zhang, Y. Gao, Z. Chen, J. Du, C. Cao, L. Kang, H. Luo, *Langmuir* **2010**, *26*, 10738.
[13] J.-P. Pouget, *C. R. Phys.* **2021**, *22*, 37.
[14] J. M. Atkin, S. Berweger, E. K. Chavez, M. B. Raschke, J. Cao, W. Fan, J. Wu, *Phys. Rev. B* **2012**, *85*, 020101.
[15] Z. Hiroi, H. Hayamizu, T. Yoshida, Y. Muraoka, Y. Okamoto, J. I. Yamaura, Y. Ueda, *Chem. Mater.* **2013**, *25*, 2202.
[16] T. Horlin, T. Niklewski, M. Nygren, *Acta Chem. Scand.* **1976**, *30*, 619.
[17] L. L. Chase, *Phys. Lett. A* **1973**, *46A*, 215.
[18] W. Brückner, U. Gerlach, H. P. Brückner, W. Moldenhauer, H. Oppermann, *Phys. Status Solidi a* **1977**, *42*, 295.
[19] Y. Wu, L. Fan, Q. Liu, S. Chen, W. Huang, F. Chen, G. Liao, C. Zou, Z. Wu, *Sci. Rep.* **2015**, *5*, 9328.
[20] Q. Lu, C. Sohn, G. Hu, X. Gao, M. F. Chisholm, I. Kylanpaa, J. T. Krogel, P. R. C. Kent, O. Heinonen, P. Ganesh, H. N. Lee, *Sci. Rep.* **2020**, *10*, 18554.
[21] H. Lu, L. Li, Z. Tang, M. Xu, Y. Zheng, M. Becker, Y. Lu, M. Li, P. Li, Z. Zhang, P. J. Klar, Y. He, *Appl. Phys. Lett.* **2023**, *123*, 042103.
[22] K. Shibuya, A. Sawa, *J. Appl. Phys.* **2017**, *122*, 015307.
[23] K. Kosuge, *J. Phys. Soc. Japan* **1967**, *22*, 551.
[24] G. Villeneuve, A. Bordet, A. Casalot, P. Hagenmuller, *Mater. Res. Bull.* **1971**, *6*, 119.
[25] G. Villeneuve, M. Drillon, P. Hagenmuller, *Mater. Res. Bull.* **1973**, *8*, 1111.
[26] E. Strelcov, A. Tselev, I. Ivanov, J. D. Budai, J. Zhang, J. Z. Tischler, I. Kravchenko, S. V. Kalinin, A. Kolmakov, *Nano Lett.* **2012**, *12*, 6198.
[27] W. Brückner, U. Gerlach, W. Moldenhauer, H. P. Brückner, B. Thuss, H. Oppermann, E. Wolf, I. Storbeck, *J. Phys. Colloq.* **1976**, *37*, C4.
[28] F. Pintchovski, W. S. Glaunsinger, A. Navrotsky, *J. Phys. Chem. Solids* **1978**, *39*, 941.
[29] Y. Zhang, W. Xiong, W. Chen, Y. Zheng, *Nanomaterials (Basel)* **2021**, *11*, 338.
[30] Y. Zheng, Z. Chen, H. Lu, Y. Cheng, X. Chen, Y. He, Z. Zhang, *Nanoscale* **2021**, *13*, 7783.
[31] A. O. Suleiman, S. Mansouri, N. Emond, B. Le Drogoff, T. Begin, J. Margot, M. Chaker, *Sci. Rep.* **2021**, *11*, 1620.
[32] B. L. Chamberland, *J. Solid State Chem.* **1973**, *46*, 215.
[33] M. Marezio, D. B. McWhan, J. P. Remeika, P. D. Dernier, *Phys. Rev. B* **1972**, *5*, 2541.
[34] J. Galy, G. Miehe, *Solid State Sci.* **1999**, *1*, 433.
[35] J. M. Longo, P. Kierkegaard, C. J. Ballhausen, U. Ragnarsson, S. E. Rasmussen, E. Sunde, N. A. Sørensen, *Acta Chem. Scand.* **1970**, *24*, 420.
[36] D. B. McWhan, M. Marezio, J. P. Remeika, P. D. Dernier, *Phys. Rev. B* **1974**, *10*, 490.
[37] S. Westman, I. Lindqvist, B. Sparrman, G. B. Nielsen, H. Nord, A. Jart, *Acta Chem. Scand.* **1961**, *1989*(15), 217.
[38] O. Frank, M. Zukalova, B. Laskova, J. Kurti, J. Koltai, L. Kavan, *Phys. Chem. Chem. Phys.* **2012**, *14*, 14567.
[39] S. P. S. Porto, P. A. Fleury, T. C. Damen, *Phys. Rev. a (3)* **1967**, *154*, 522.
[40] I. R. Beattie, T. R. Gilson, *Proc. R. Soc. Lond. A* **1968**, *307*, 407.
[41] U. Balachandran, N. G. Eror, *J. Solid State Chem.* **1982**, *42*, 276.
[42] F. Ureña-Begara, A. Crunteanu, J.-P. Raskin, *Appl. Surf. Sci.* **2017**, *403*, 717.
[43] R. Srivastava, L. L. Chase, *Phys. Rev. Lett.* **1971**, *27*, 727.
[44] C. Marini, E. Arcangeletti, D. Di Castro, L. Baldassare, A. Perucchi, S. Lupi, L. Malavasi, L. Boeri, E. Pomjakushina, K. Conder, P. Postorino, *Phys. Rev. B* **2008**, *77*, 235111.
[45] M. K. Dietrich, F. Kuhl, A. Polity, P. J. Klar, *Appl. Phys. Lett.* **2017**, *110*, 141907.
[46] H. Lu, L. Chen, R. Cao, X. Tao, X. Wang, M. Li, P. Li, Y. Lu, P. J. Klar, Y. He, *Appl. Phys. Lett.* **2020**, *116*, 192103.
[47] W. Hayes, R. Loudon, *Scattering of light by crystals*, Wiley, New York **1978**.
[48] P. Schilbe, *Phys. Rev. B Condens. Matter* **2002**, *316*, 600.

SUPPORTING INFORMATION

Additional supporting information can be found online in the Supporting Information section at the end of this article.

How to cite this article: F. Kuhl, H. Lu, M. Becker, L. Chen, Y. Zheng, A. Polity, Z. Zhang, Y. He, P. J. Klar, *J Raman Spectrosc* **2024**, *55*(8), 923. https://doi.org/10.1002/jrs.6684